



Transition metal and nitrogen-doped mesoporous carbons as cathode catalysts for anion-exchange membrane fuel cells

Jaana Lilloja ^a, Elo Kibena-Pöldsepp ^a, Ave Sarapuu ^a, Maike Käärik ^a, Jekaterina Kozlova ^b, Päärn Paiste ^c, Arvo Kikas ^b, Alexey Treshchalov ^b, Jaan Leis ^a, Aile Tamm ^b, Vambola Kisand ^b, Steven Holdcroft ^d, Kaido Tammeveski ^{a,*}

^a Institute of Chemistry, University of Tartu, Ravila 14a, 50411 Tartu, Estonia

^b Institute of Physics, University of Tartu, W. Ostwald Str. 1, 50411 Tartu, Estonia

^c Institute of Ecology and Earth Sciences, University of Tartu, Vanemuise 46, 51014 Tartu, Estonia

^d Department of Chemistry, Simon Fraser University, 8888 University Drive, Burnaby, BC V5A 1S6, Canada



ARTICLE INFO

Keywords:

Alkaline anion-exchange membrane fuel cell
Electrocatalysis
Mesoporous carbon
Non-precious metal catalysts
Oxygen reduction

ABSTRACT

Transition metal- and nitrogen-doped mesoporous carbons are prepared, characterised, and used as oxygen reduction reaction (ORR) electrocatalysts in an anion exchange membrane fuel cell (AEMFC). Novel mesoporous carbon (MPC) based engineered catalyst support is doped using high-temperature pyrolysis in the presence of metal acetate(s) and 1,10-phenanthroline (nitrogen source). Three transition metals are used to prepare materials with the following metal compositions: Fe, Co, CoFe, FeMn, and CoMn. Physico-chemical characterisation shows the success of doping with similar morphology and textural properties of all materials. The rotating ring-disc electrode experiments in alkaline solution show that all five catalysts exhibit good electrocatalytic activity towards the ORR, with Fe-N-MPC, CoFe-N-MPC and FeMn-N-MPC being best-performing materials with excellent stability. The HO_2^- yield depends on the metal composition with Fe-N-MPC and FeMn-N-MPC giving the lowest percentage. The latter two are employed in the AEMFC and reach power densities of 473 and 474 mW cm^{-2} , respectively.

1. Introduction

Hydrogen is believed to become an essential player in the energy field as it is clean, cost-efficient, and easily producible fuel [1–4]. Although several automobile makers are already producing proton-exchange membrane fuel cell (PEMFC) powered cars for commercial usage, there are some limitations to their wide availability, namely the price and excessive usage of precious metals in the fuel cell [5–8]. Platinum-based catalyst materials are used for both the anodic hydrogen oxidation reaction (HOR) and cathodic oxygen reduction reaction (ORR) in PEMFCs as they are the best performing and most stable ones in acidic conditions so far [5,9]. There is extensive research going on to find replacements for Pt-based materials for acidic media [10–12], but an option is also to switch the medium for alkaline [13,14]. The higher pH is not that harsh for non-precious metal-based materials and would also remove the need for acid-resistant stack hardware, thus reducing the price of these [13]. Such alkaline operating fuel cells,

namely anion-exchange membrane fuel cells (AEMFCs) have been investigated for quite some time, but the largest breakthrough has come in last decade with the development of mechanically and chemically stable anion-exchange membranes (AEMs) [14–16].

With the possible AEMs being available, the focus is still on finding more sustainable and cheaper electrocatalysts. For the anodic HOR unfortunately, the replacement of platinum group metals (PGM) used is rather difficult as even PGMs struggle in alkaline conditions and non-PGM ones have still not demonstrated good enough results [17–19]. In contrast, for the cathodic ORR, the non-PGM catalyst materials have shown great promise [20]. So, by replacing the ORR electrocatalyst with non-PGM material and reducing the PGM content on the anode side, the fuel cell could become more feasible and sustainable.

As a replacement for ORR catalysts, different carbon-based materials could be used. However, pristine carbon materials show low electrocatalytic activity for the ORR [21–23] and thus need modifying, for instance doping with heteroatoms, such as N [24–27], S [28–30], P

* Corresponding author.

E-mail address: kaido.tammeveski@ut.ee (K. Tammeveski).

[31–34], and non-PGMs [20,35–37]. From these, transition metal-containing N-doped carbon (M–N–C) materials stand out as the most promising ones as they have shown comparable or even superior performance to the state-of-the-art Pt/C [20,38–42]. The high ORR activity of M–N–C (M=Fe, Co, Mn) materials is thought to come from the presence of metal-coordinated to nitrogen moieties (M–N_x, where x = 2 or 4), nitrogen-containing species (e.g. pyridinic-N), and/or metal carbide particles covered with (nitrogen doped) carbon layer [39,43,44].

To obtain the M–N_x active centres, precursors with the inner N₄ coordination around the transition metal centre, such as metal phthalocyanines and porphyrins, have been widely used as they are cheaper than Pt, but give comparable ORR activity in alkaline media. In early works, physical adsorption of these MN₄ macrocycles onto the carbon substrate was employed, however, to overcome the lack of stability, the high-temperature pyrolysis is needed to produce the catalysts. The ORR activity of these materials is determined by the redox potential of the central metal ion, which subsequently depends on the electron donating/withdrawing capability of the carbon substrate [45–50]. However, these M–N_x active sites can also be created by pyrolysing the carbon substrates in the presence of precursors that do not contain M–N_x moieties, thus allowing the use of even simpler and cheaper nitrogen sources (e.g. melamine, dicyandiamide) and transition metal salts (e.g. iron chloride, cobalt nitrate) [20,40,41].

To prepare the M–N–C type catalyst materials for the ORR, both iron and cobalt have been widely studied as prospective transition metals [51–58]. Despite the good performances, such materials often have some drawbacks – cobalt-based materials exhibit rather high peroxide yield during the ORR [41,52,59], and while iron-based catalysts have lower HO₂[–] yield [58–61], they are still subject to Fenton reaction (especially at low pH) [62,63]. One possible way to improve the results is to make bimetallic catalyst materials, which have shown synergistic effects of Fe-N₄ and Co-N₄ centres [64,65]. To make bimetallic Fe and Co based materials, an option is also to incorporate another transition metal, namely manganese, as Mn has shown to increase the ORR activity and exhibit excellent stability in combinations with Fe or Co [63,66–68]. Moreover, both Mn–N–C and Fe–N–C materials are considered to promote four-electron pathway for the ORR, while Co–N–C is thought to promote two-electron pathway, leading to peroxide production [59].

When making M–N–C type catalyst material, a key component is the carbon support. The role of the catalyst support is to: (i) provide good electrical conductivity with high surface area, (ii) allow the reactants to access the active sites via the pore structure and (iii) provide corrosion stability in harsh conditions [69]. The choice for carbon supports is wide [20,69,70], but to obtain catalyst material with uniform structure, the support itself should already have feasible structure. For the fuel cell application, the suitable pore size distribution is as important as the high surface area. The good materials should have mesopores (2–50 nm in diameter) present, which are useful for mass transport in the catalyst layer, as micropores (<2 nm) and any active sites located there tend to be covered with ionomer during the fuel cell application [61,71].

Herein, five different M–N–C type ORR catalyst materials are synthesised and characterised. A novel and commercially available mesoporous engineered catalyst support based on carbon (from Pajarito Powder, LLC) is the basis for all materials. This material has a well-defined and uniform mesoporous structure with pore sizes predominantly 7 and 35 nm, which offers plenty of pathways for reactants to reach the active sites. This is the first report on doping this mesoporous carbon-based support with transition metals and nitrogen using simple and cost-efficient high-temperature pyrolysis method. 1,10-phenanthroline is used as nitrogen source as it is known to form complexes with transition metal salts, leading to the formation of M–N_x species in the final catalyst material [72,73]. As transition metals, iron, cobalt, and manganese are employed – iron and cobalt monometallic samples are compared with bimetallic ones to see if combining two metals (e.g. CoFe, FeMn, CoMn) leads to improved performance due to proposed synergistic effects as mentioned before. All prepared catalyst materials

undergo physico-chemical characterisation as well as their electrocatalytic activity towards the ORR is tested using the rotating ring-disc electrode method. This enables a reliable comparison between mono- and bimetallic Co, Fe and Mn based materials, as the catalyst preparation and testing is done under the same conditions. The best-performing M–N–C materials are employed as cathode catalysts in an AEMFC.

2. Experimental

2.1. Catalyst synthesis

Mesoporous Engineered Catalyst Support based on carbon (product code: ECS-004601, herein designated as MPC) was purchased from Pajarito Powder, LLC. The MPC material was prepared using VariPore™ method with the aim to contain both smaller (ca. 7 nm) and larger (ca. 35 nm) mesopores. 1,10-phenanthroline (purity >99%, Acros Organics) was used as nitrogen precursor. As the metal precursors iron(II) acetate (purity 95%, Sigma-Aldrich), cobalt(II) acetate (purity >98%, Alfa Aesar), and manganese(II) acetate tetrahydrate (purity >99%. Sigma-Aldrich) were used.

In the first step of synthesis of catalyst materials, the transition metal acetates together with 1,10-phenanthroline were dissolved in ethanol. Typical amounts were: 12.5 mg of 1,10-phenanthroline, 1 or 2 mg of iron(II) and cobalt(II) acetate and 1.4 mg of manganese(II) acetate tetrahydrate. The transition metal acetates were taken in such amount that the total mass of the metals would correspond to 1 wt% of the MPC, and in case of bimetallic materials the mass of both metals would be equal.

This mixture of metal acetate(s) and 1,10-phenanthroline was treated in an ultrasonic bath (Branson 1510E-MTH, Bransonic®) for 30 min. Lastly, 50 mg of MPC was added, followed by sonication for at least 60 min until a uniform dispersion was achieved. The prepared liquid mixture was dried overnight in an oven at 60 °C. The obtained dry powder was pyrolyzed using a small tube furnace (EST 12/300B, Carbolite Ltd.) in an inert atmosphere (N₂, 99.999%, Linde Gas). The sample was inserted to the heating zone at 800 °C, kept there for 1 h and then quickly removed, thus obtaining the catalyst material.

According to the metal precursors used, the electrocatalyst materials are designated as follows: Fe-N-MPC, Co-N-MPC, CoFe-N-MPC, FeMn-N-MPC, and CoMn-N-MPC.

2.2. Physico-chemical characterisation

For the physico-chemical characterisation of catalyst materials scanning electron microscopy (SEM) with energy dispersive X-ray analysis (EDX), N₂ physisorption, X-ray photoelectron spectroscopy (XPS), microwave plasma atomic emission spectroscopy (MP-AES), Raman spectroscopy and scanning transmission electron microscopy (STEM) were applied. Detailed experimental descriptions of these techniques can be found in the [Supplementary material](#).

2.3. Electrochemical measurements

The electroreduction of oxygen was studied using the rotating ring-disc electrode (RRDE) method. The electrochemical measurements were conducted in 0.1 M KOH (≥85%, Sigma-Aldrich) solution at room temperature using a three-electrode setup. Before the experiments, the electrolyte solution was saturated with O₂ (99.999%, Linde Gas) or Ar (99.999%, Linde Gas) with the respective gas flow being maintained over the solution during the experiment as well. As a working electrode, a fixed-disc tip glassy carbon (GC) disc/Pt ring electrode (Pine Research, USA) was used. The GC disc with the geometric area of 0.164 cm² was coated by the respective catalyst with a loading of 0.4 mg cm^{–2}. The preparation of electrodes was done according to a well-established procedure and the description of it can be found in the [Supplementary material](#). As a reference electrode, saturated calomel electrode (SCE) connected through a salt bridge was used, but the potentials were

converted to the reversible hydrogen electrode (RHE) using the equation: $E_{\text{RHE}} = E_{\text{SCE}} + 0.241 \text{ V} + 0.059 \text{ V} \times \text{pH}$. The auxiliary electrode was a carbon rod (diameter of 3 mm) separated from the working electrode compartment via a glass frit.

Electrochemical experiments were conducted on PGSTAT30 Autolab potentiostat/galvanostat (Eco Chemie B.V., The Netherlands) together with MSRX speed controller and an AFMSRX rotator (Pine Research, USA) used for the RRDE measurements. Experiments were controlled using General Purpose Electrochemical System (GPES) software.

For the detection of hydroperoxide anion (HO_2^-) formation during the RRDE measurements, the Pt ring electrode (collection efficiency 0.22) was kept at a constant potential of 1.55 V. The ring electrode was electrochemically cleaned before each measurement by applying at least three potential cycles from 0.05 to 1.65 V at 100 mV s⁻¹.

The RRDE data were used to calculate the peroxide yield and the electron transfer number. To calculate the percentage yield of HO_2^- formation at the disc electrode, Eq. (1) was used:

$$\% \text{HO}_2^- = \frac{\frac{2I_r}{N}}{I_d + \frac{I_r}{N}} \times 100\% \quad (1)$$

where I_d is the disc current, I_r is the ring current, and N is the collection efficiency of the ring electrode. The number of electrons transferred per O_2 molecule (n) was calculated from the RRDE data using Eq. (2):

$$n = \frac{4I_d}{I_d + \frac{I_r}{N}} \quad (2)$$

The mass activity (MA) of catalyst materials for O_2 reduction was calculated by Eq. (3):

$$\text{MA} = \frac{I_k}{m} \quad (3)$$

where I_k is the kinetic current at a certain potential and m is the mass of the catalyst material on the electrode. From the RRDE data, the I_k was found using the Koutecky-Levich equation:

$$\frac{1}{I} = \frac{1}{I_k} + \frac{1}{I_d} \quad (4)$$

where I is the measured current at a certain potential and I_d is the diffusion-limited current.

The effect of cyanide ions was tested in 0.1 M KOH containing 10 mM NaCN (97%, Sigma-Aldrich). The stability test was carried out by applying 10,000 cycles in the potential range from 1.1 to 0.6 V at 200 mV s⁻¹ in O_2 -saturated 0.1 M KOH solution. The ORR polarisation curves were recorded before and after the potential cycling at an electrode rotation rate (ω) of 960 rpm between 1.1 and -0.2 V and a potential scan rate (ν) of 10 mV s⁻¹.

For comparison purposes, both the unmodified MPC and commercial 20 wt% Pt catalyst supported on Vulcan carbon XC-72 (E-TEK, Inc.) were tested employing the RRDE technique.

2.4. Anion-exchange membrane fuel cell (AEMFC) tests

To construct the membrane-electrode assembly (MEA) for AEMFC, the gas-diffusion layers (GDL, Sigracet 39 BCE) were coated with the catalyst materials. To make a catalyst suspension for the cathode, 12.5 mg of M-N-MPC material was dispersed in 1340 μL of methanol, 391 μL of Milli-Q water and 130 μL of hexamethyl-p-terphenyl-poly(methylbenzimidazolium) (HMT-PMBI) [74] ionomer solution (3 wt% in methanol). For comparison, a commercial Pt/C (46 wt%, Tanaka Kikinzoku Kogyo, Japan) was also used as the cathode catalyst: 5.4 mg of Pt/C was dispersed in 580 μL of methanol, 169 μL of Milli-Q water and 56 μL of ionomer solution. For the anode, a commercial Pt-Ru/C catalyst (50:25:25, Alfa Aesar) was applied with the suspension consisting of 6.67 mg of Pt-Ru/C dispersed in 689 μL of methanol, 196 μL of

Milli-Q water and 49 μL of HMT-PMBI ionomer solution (3 wt% in methanol). All prepared suspensions were sonicated for 1 h in an ultrasonic bath, followed by drop casting onto the corresponding GDL. The electrodes were dried under vacuum in an oven at 60 °C. The final catalyst loading on the cathode was 2 mg cm⁻² (or 0.4 mg_{Pt} cm⁻² for Pt/C) and 0.8 mg_{Pt-Ru} cm⁻² on the anode. The electrodes were immersed in 3 M KOH ($\geq 85\%$, Lach-Ner) solution 24 h prior to testing. The HMT-PMBI membrane ([74], thickness 10 μm) was immersed in 3 M KOH for 96 h before testing with the fresh solution provided after every 24 h. The electrodes and the membrane were pressed together into a 5 cm² cell (Fuel Cell Technologies Inc., USA) with silicone gasket by applying a torque of 9 Nm. Greenlight Fuel Cell Test Station (G50 Fuel Cell System, Hydrogenics, Canada) was used to conduct the single-cell AEMFC test. Humidified (relative humidity 50%) O_2 (99.95%, Linde Gas) and H_2 (99.999%, Linde Gas) gases at 60 °C were fed to the system using a flow rate of 1.0 NLPM. The applied backpressure was 200 kPa.

3. Results and discussion

3.1. Physico-chemical characterisation of M-N-MPC catalysts

SEM technique was used to study the morphology of the prepared materials as well as MPC support material. SEM micrographs are shown in Fig. 1 and S1. The MPC support material (Fig. 1a-c) has a rather homogeneous morphology with high roughness and highly porous nature. After doping the material using different metal compositions (Fig. 1d-f, S1), no noticeable differences can be seen from SEM images as the M-N-MPC materials were also mostly homogeneous and had a high roughness at different scales. From the lower magnification images, some larger particles with smoother surface were visible in case of all samples. These results show that doping with metals using high-temperature pyrolysis has not changed the carbon morphology much, suggesting that the feasible structure of starting engineered catalyst support is still present.

The morphology of three iron-based materials was further studied using STEM technique with bright field (BF) and high-angle annular dark field (HAADF) images together with EDX mapping (see Fig. 2 and S2). From the STEM images it is visible that the materials are indeed highly porous and rather homogeneous. Some graphitic carbon structures comprising of approximately 3–4 graphene-like layers can be seen from higher-magnification images in Fig. 2c, S2c and S2i. The EDX mapping (Fig. 2e-f) shows that the nitrogen and corresponding metals are uniformly distributed in the catalyst materials and that the metal particles are predominantly rather small, some of them difficult to distinguish, which might suggest that metals can be atomically dispersed in the M-N-MPC materials. The latter is also supported by the higher magnification HAADF-STEM images of FeMn-N-MPC (Fig. S3) where well-distributed brighter spots correspond to transition metal atoms.

N_2 physisorption studies were conducted to analyse the textural properties of the prepared M-N-MPC materials. The results are summarised in Table 1, Fig. 3a and Fig. S4. The shape of the isotherms (Fig. S4) was rather similar in all samples and exhibited H3 hysteresis according to IUPAC [75]. The specific surface area (SSA) of MPC material was 814 m² g⁻¹ and around 500–600 m² g⁻¹ in M-N-MPC catalyst materials, meaning that during doping some of the existing pores were blocked, thus resulting in the reduced SSA. The latter also applies to the total pore volume (V_{tot}) as it decreased from 1.51 cm³ g⁻¹ in MPC to 1.22–1.35 cm³ g⁻¹ in M-N-MPC samples. There are two distinct maxima in all pore-size distribution graphs (Fig. 3a) corresponding to the smaller and larger mesopores in the diameter range of 7–8 nm and 25–35 nm, respectively. This predominantly mesoporous nature with different pore sizes could have a positive effect on the transport of the reactants and products and thus improve the AEMFC performance [76].

The first-order Raman spectra of the MPC and M-N-MPC catalyst materials are presented in Fig. 3b. The Raman spectra of all the materials are very similar with the presence of wide bands, namely the graphitic carbon (G, $\sim 1590 \text{ cm}^{-1}$) and disordered carbon (D1, $\sim 1350 \text{ cm}^{-1}$)

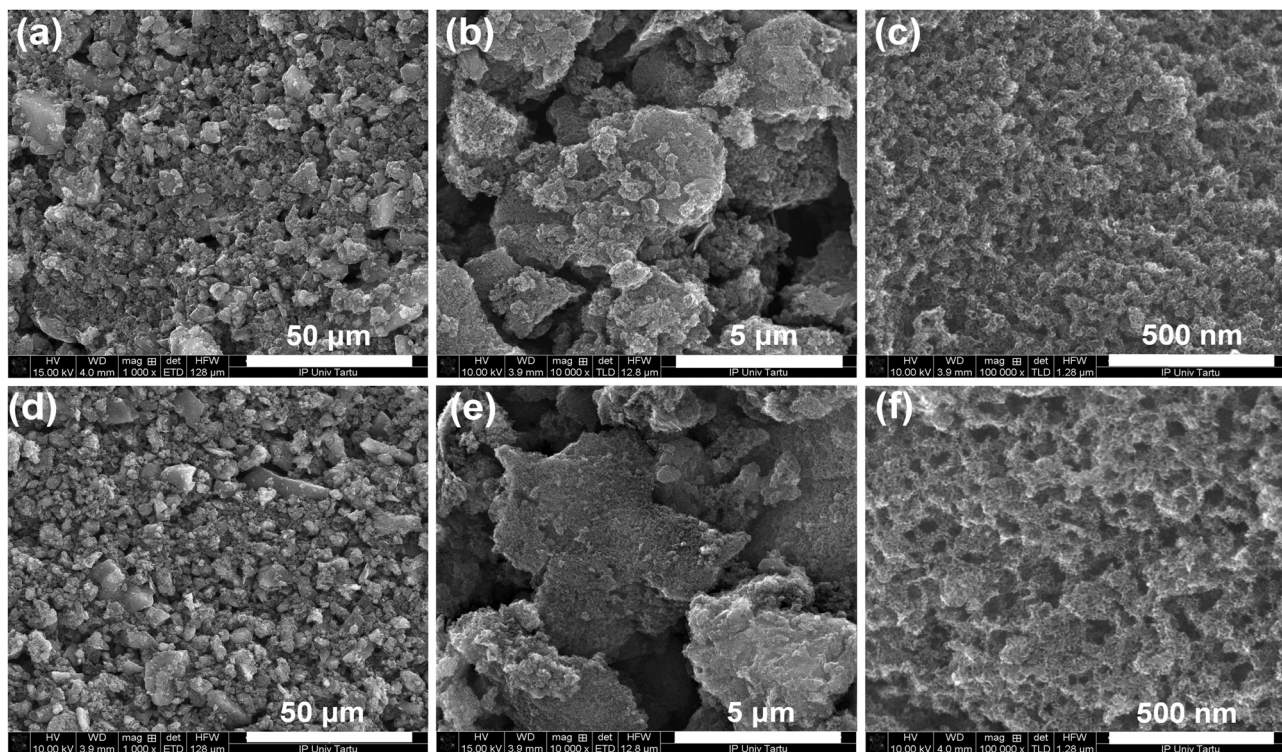


Fig. 1. SEM micrographs for MPC (a–c), and FeMn-N-MPC material (d–f).

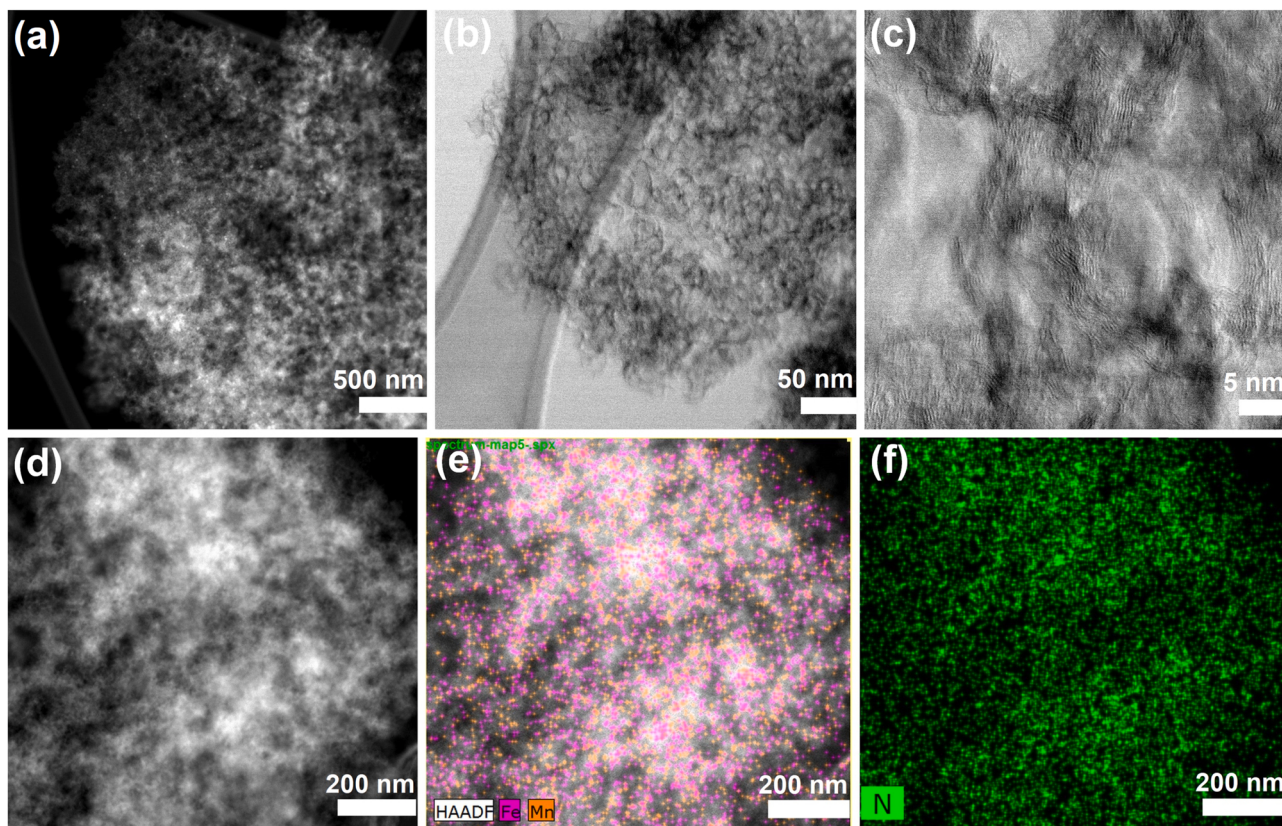


Fig. 2. (a, d) HAADF-STEM images, (b–c) BF-STEM images, (e) EDX mapping (HAADF-EDX) for iron and manganese and (f) EDX map of nitrogen of FeMn-N-MPC.

Table 1Specific surface area (SSA) and total pore volume (V_{tot}) for MPC and M-N-MPC samples.

	MPC	Fe-N-MPC	Co-N-MPC	CoFe-N-MPC	FeMn-N-MPC	CoMn-N-MPC
SSA ($\text{m}^2 \text{ g}^{-1}$)	814	584	535	571	583	613
V_{tot} ($\text{cm}^3 \text{ g}^{-1}$)	1.51	1.33	1.24	1.22	1.24	1.35

peaks. The G peak is characteristic for carbon materials and is related to the in-plane stretching of the C–C bonds at sp^2 sites. The presence of D1 peak, however, indicates that there is disorder in the structure, meaning the materials are quite amorphous [77]. The fitting of the Raman spectra was done according to the suggestions given by Sadezky et al. [78] (see details in the [Supplementary material](#)). The ratio of the integrated areas of D1 and G peaks, $I_{\text{D1}}/I_{\text{G}}$, was 1.34 for MPC and increased to 1.43 in all other samples. The widths of D1 and G bands, which increase with the degree of disorder in the graphitic lattice [79], were more or less the same in all samples being 130 and 81 cm^{-1} , respectively. High $I_{\text{D1}}/I_{\text{G}}$ values as well as wide D1 and G bands indicate that there is a significant level of disorder together with defects present in the prepared catalyst materials.

The synthesised M-N-MPC catalyst materials were further analysed for their bulk transition metal content and surface elemental composition using the MP-AES, SEM-EDX and XPS techniques. The MP-AES results in [Table S1](#) show that the bulk metal content was close to 1 wt% in all materials, and that in bimetallic materials, both added transition metals constitute to around the half of the overall metal content. Similar metal contents were obtained with the SEM-EDX method ([Table S2](#)), which also showed the presence of small amount of silica in starting

MPC and M-N-MPC materials (mostly from silica template used in manufacturing of MPC supports) and that the nitrogen content has indeed increased after doping. These results indicate that doping the MPC material with metals using high-temperature pyrolysis has been a success with all three transition metals (Fe, Co and Mn) and their combinations.

XPS analysis was applied to examine the surface elemental composition of the prepared M-N-MPC catalyst samples as the accessible ORR active sites are located there. The data obtained are presented in [Fig. 4](#), [S5](#) and [S6](#) as well as in [Tables 2](#) and [3](#). The XPS results ([Fig. S5](#), [Table 2](#)) indicate that in case of all five samples C, N, O as well as the added

Table 2

Surface elemental composition of M-N-MPC materials (at%) by XPS analysis.

Catalyst material	C	N	O	Fe	Co	Mn
Fe-N-MPC	95.5	2.3	2.1	0.1	–	–
Co-N-MPC	95.7	2.4	1.7	–	0.2	–
CoFe-N-MPC	95.6	2.4	1.8	0.1	0.1	–
FeMn-N-MPC	95.8	2.3	1.7	0.1	–	0.1
CoMn-N-MPC	95.7	2.2	1.9	–	0.1	0.1

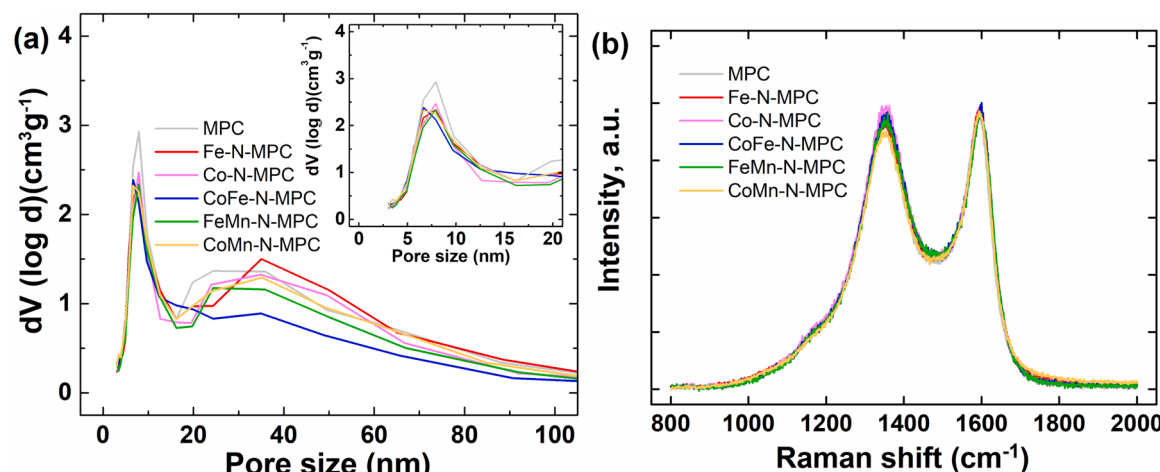


Fig. 3. (a) Pore size distributions and (b) Raman spectra for MPC and M-N-MPC materials.

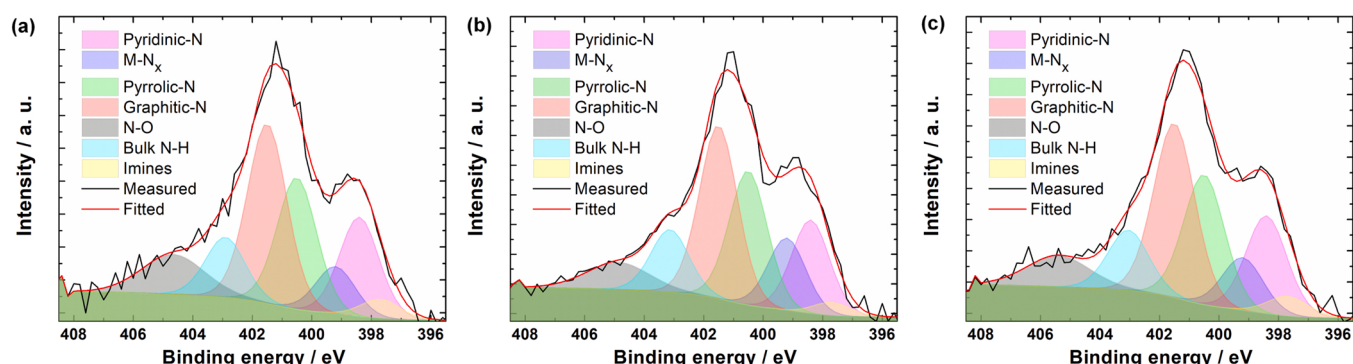


Fig. 4. N1s high resolution XPS spectra for (a) Fe-N-MPC, (b) CoFe-N-MPC and (c) FeMn-N-MPC samples.

Table 3

Relative concentration (%) of N species on M-N-MPC materials by XPS analysis.

N species	Fe-N-MPC	Co-N-MPC	CoFe-N-MPC	FeMn-N-MPC	CoMn-N-MPC
Pyridinic-N	16.5	17.5	15.6	16.9	17.0
M-N _x	7.8	11.5	12.2	9.1	9.2
Pyrrolic-N	22.2	23.8	22.8	22.1	24.9
Graphitic-N	30.0	29.4	29.1	29.9	28.6
N-O	10.4	5.5	7.6	8.2	8.8
Bulk N-H	10.0	10.2	10.6	10.4	9.2
Imine	3.1	2.1	2.1	3.4	2.3

respective metals (Fe, Co, Mn or two of them), are present on the surface of the catalyst materials. The overall surface nitrogen content was almost the same in all M-N-MPC materials and ranged from 2.2 to 2.4 at %. For determination of the type of N species present in the prepared catalysts, the detailed XPS spectra of the N1s region was deconvoluted into seven peaks with the corresponding results shown in Fig. 4, Fig. S6 and Table 3. The deconvoluted N1s peaks and used binding energies are as follows: imine \sim 397.7 eV, pyridinic-N \sim 398.4 eV, M-N_x \sim 399.2 eV, pyrrolic-N \sim 400.5 eV, graphitic-N \sim 401.5 eV, N-O \sim 404.9 eV, and bulk N-H \sim 402.9 eV. Pyridinic-N, pyrrolic-N and graphitic-N were present in the highest amounts, but there was also a noticeable concentration of metal-coordinated nitrogen species (M-N_x). This coexistence of different moieties, which is common in materials synthesised using high-temperature pyrolysis, could be beneficial, as each of them is responsible for certain steps in the ORR. Kabir et al. have claimed that HO₂⁻ is formed on graphitic-N in the first step, followed by OH⁻ production in the second step on pyridinic-N, and pyrrolic-N catalyses the $2 \times 2e^-$ reduction of O₂ [80]. Additionally, Lai et al. have proposed that the electrocatalytic activity of catalysts towards the ORR depends on the graphitic-N and pyridinic-N content with the first one influencing the diffusion-limited currents and the latter improving the onset potential [81]. The metal-coordinated nitrogen sites are considered to be active for full reduction of oxygen via either direct $4e^-$ or $2 \times 2e^-$ mechanism [82].

3.2. Oxygen reduction reaction (ORR) on M-N-MPC catalysts

The initial assessment of the prepared catalyst materials' activity towards the ORR was done using the RRDE method in O₂-saturated 0.1 M KOH aqueous solution at 960 rpm. The obtained disc current densities and ring currents are shown in Fig. 5 with the results compiled as well in Table 4. It should be noted that the peak at ca. 0.8 V in some

Table 4

The ORR parameters determined for electrocatalyst materials in 0.1 M KOH solution.

	E_{onset}/V^*	$E_{1/2}/V^*$	MA at 0.9 V/A g ⁻¹	%HO ₂ ⁻	n
MPC	0.90	0.80	0.4	24–46	3.0–3.5
Fe-N-MPC	0.99	0.89	7.7	1–12	3.8–4.0
Co-N-MPC	0.92	0.84	1.1	21–30	3.4–3.6
CoFe-N-MPC	1.00	0.90	10.1	11–21	3.5–3.7
FeMn-N-MPC	0.98	0.89	7.4	1–12	3.8–4.0
CoMn-N-MPC	0.94	0.84	1.4	28–36	3.3–3.5
Pt/C (20 wt %)	1.00	0.90	9.7 (48.5 A g _{Pt} ⁻¹)	0–8	3.9–4.0

*Standard deviation is within 3 mV

materials corresponds to the reduction of oxygen, which was trapped inside the porous catalyst layer. The starting MPC material had the lowest ORR performance with the onset potential for O₂ reduction (E_{onset} , specified as the potential where the ORR current density reaches -0.1 mA cm^{-2}) being 0.90 V, the half-wave potential ($E_{1/2}$) being 0.80 V, and the lowest diffusion-limited current value. All five prepared catalyst materials showed better performance than the pristine MPC. Among them, the Co-N-MPC and CoMn-N-MPC catalysts had somewhat inferior performance while exhibiting $E_{1/2}$ of 0.84 V. On the other hand, the materials containing iron, namely Fe-N-MPC, CoFe-N-MPC, and FeMn-N-MPC all showed impressive ORR activity similar to that of the commercial Pt/C (20 wt%) with E_{onset} and $E_{1/2}$ of around 1.0 and 0.9 V, respectively. In addition, the mass activity (MA) of the catalyst materials was calculated from the RRDE data (Fig. 5a) using Eqs. (3) and (4) and the obtained values at 0.9 V are shown in Table 4. Highest MA value was found for CoFe-N-MPC material, followed by FeMn-N-MPC and Fe-N-MPC catalysts. The obtained results are comparable to that of Pt/C material (when considering its carbon mass as well) and the MA values over 7 A g⁻¹ place these three catalysts among the best-performing M-N-C materials so far reported in the literature [62,83,84].

To obtain more information on the ORR pathway, the respective ring currents were also collected (Fig. 5b), and by using the data given in Fig. 5 and applying Eqs. (1) and (2), the yield of HO₂⁻ formation and the number of electrons transferred were calculated with results presented in Fig. 6 and Table 4. Some of the same tendencies that were visible from the ORR polarisation curves are applicable herein: the MPC had the poorest performance by having the HO₂⁻ formation of around 40% in a wide range of potentials, followed by Co-N-MPC and CoMn-N-MPC with 21–36%. While the remaining three catalysts showed almost identical values of E_{onset} and $E_{1/2}$, the CoFe-N-MPC material had higher yield of hydroperoxide anions (11–21%) than Fe-N-MPC and FeMn-N-MPC,

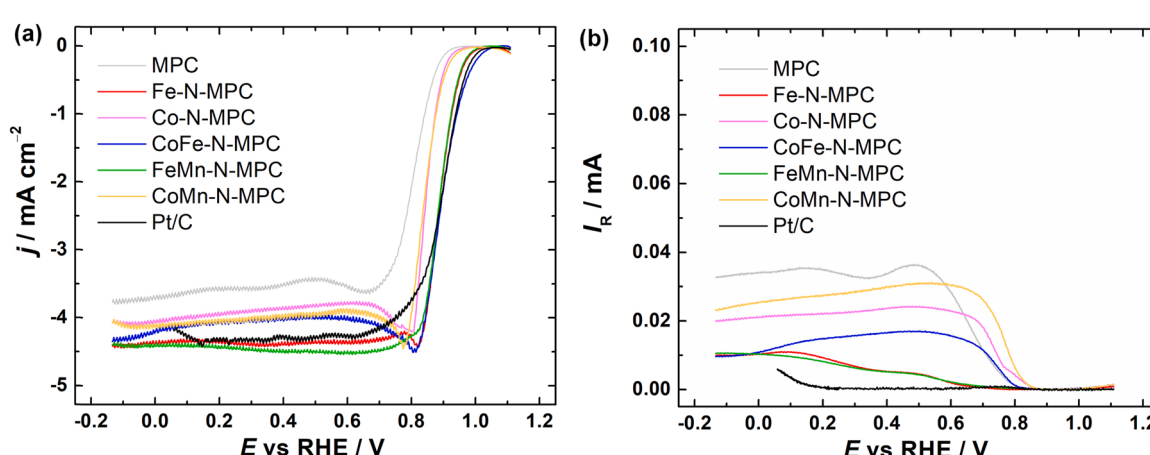


Fig. 5. RRDE results for the ORR in O₂-saturated 0.1 M KOH solution on MPC, M-N-MPC, and Pt/C catalysts. (a) disc current densities, (b) ring currents. $\omega = 960 \text{ rpm}$, $\nu = 10 \text{ mV s}^{-1}$.

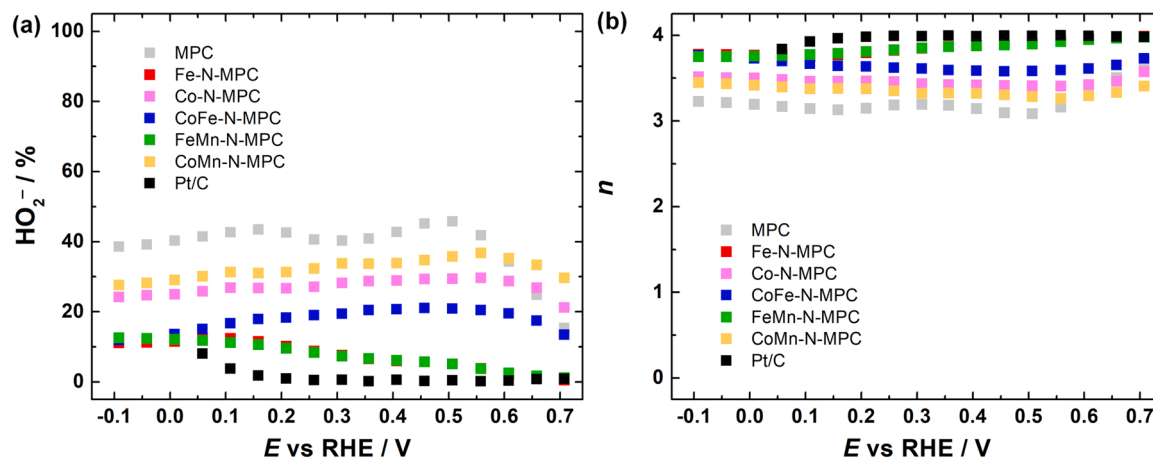


Fig. 6. (a) The percentage yield of HO_2^- formation and (b) the value of n as a function of potential for oxygen reduction on MPC, M-N-MPC, and Pt/C catalysts in O_2 -saturated 0.1 M KOH solution. Data derived from Fig. 5.

which both had low % HO_2^- of 1–12%. The latter two were also closest to the Pt/C in that sense and the n value was close to 4 for these catalysts, being less than four for other materials. These results indicate that the ORR on M-N-MPC catalyst materials proceeds mostly via a $2 \times 2e^-$ pathway, where hydroperoxide anions are formed as an intermediate with most of these being further reduced to OH^- (n is between 3 and 4).

The three best-performing catalyst materials were further tested for their stability and tolerance to cyanide poisoning. The M-N-MPC materials showed excellent electrocatalytic activity and it was evident that the transition metal addition improved the results significantly. To have a better understanding of the role of transition metal-containing active sites in the ORR, the polarisation curves were recorded in the presence of NaCN in the electrolyte solution as it is known that CN^- anions strongly adsorb to M-N_x sites, thus preventing their access to O_2 molecules, which hinders the ORR activity [85,86]. Fig. S7 shows that addition of CN^- significantly decreases the ORR activity of the catalysts as the half-wave potentials shift negative by 68, 97 and 73 mV for Fe-N-MPC, CoFe-N-MPC and FeMn-N-MPC catalysts, respectively. These test

results confirm the presence of active M-N_x centres in the M-N-MPC catalysts as was also evident from the XPS results. The remaining ORR activity can be attributed to the pyridinic-N, pyrrolic-N and graphitic-N centres, which are present in rather high amounts in the materials.

As good durability is essential for fuel cell application, then the catalyst materials were tested for their stability. The short-term stability testing involved potential cycling for 10,000 times with the ORR polarisation curves as well as respective ring currents in RRDE were recorded before and after (Fig. 7). In case of all three materials, namely Fe-N-MPC, CoFe-N-MPC, and FeMn-N-MPC, the electrocatalytic activity remained virtually the same as no significant differences can be seen between the initial ORR polarisation curve and the one obtained after 10,000 potential cycles. Both the Fe-N-MPC and FeMn-N-MPC catalysts had a negative shift of 6 mV in terms of half-wave potential, while CoFe-N-MPC had $\Delta E_{1/2}$ of 8 mV. Additionally, the yield of HO_2^- can also be compared before and after short-term stability test (Fig. 7d–f). A slight increase in the HO_2^- yield was observed with Fe-N-MPC and CoFe-N-MPC catalysts while for the FeMn-N-MPC material it remained

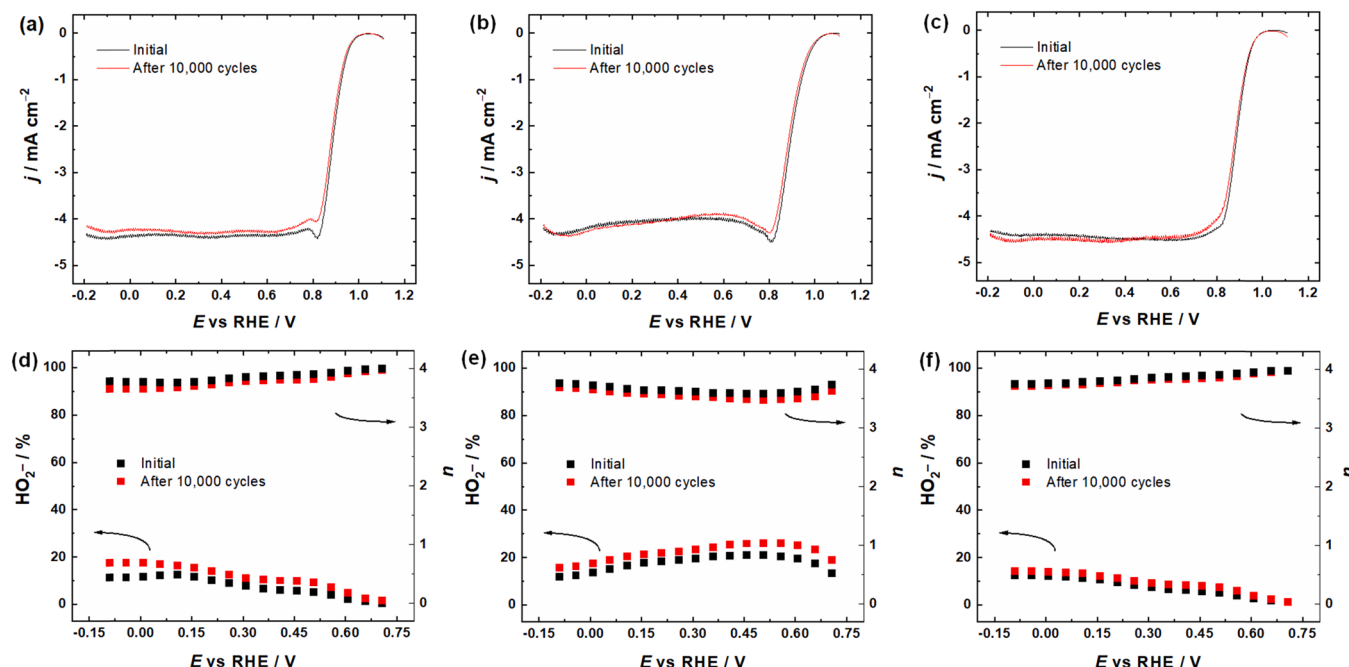


Fig. 7. (a–c) ORR polarisation curves and (d–f) the percentage yield of HO_2^- formation and the value of n as a function of potential for (a, d) Fe-N-MPC, (b, e) CoFe-N-MPC and (c, f) FeMn-N-MPC catalyst materials in O_2 -saturated 0.1 M KOH solution before and after 10,000 potential cycles ($\omega = 960$ rpm, $\nu = 10$ mV s⁻¹).

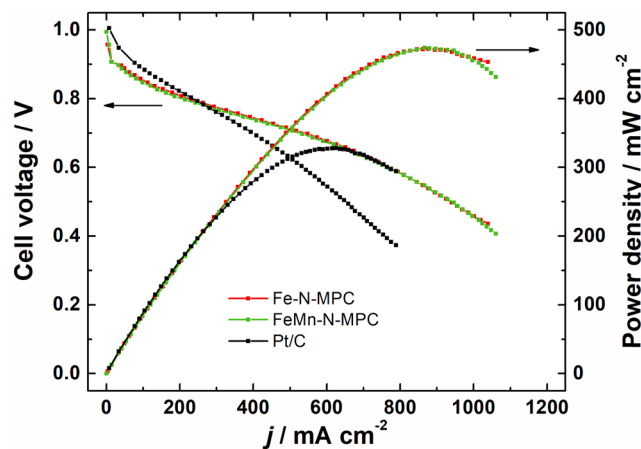


Fig. 8. Polarisation and power density curves for H_2/O_2 AEMFCs. Cathode catalyst: Fe-N-MPC, FeMn-N-MPC or Pt/C; anode catalyst: Pt-Ru/C and AEM: HMT-PMBI. $T = 60^\circ\text{C}$.

practically the same.

According to the RRDE results, the M-N-MPC catalyst materials show very good electrocatalytic performance. When comparing the transition metals used, it can be concluded that:

- iron doping (Fe-N-MPC) enhances the electrocatalytic activity more than cobalt doping (Co-N-MPC);
- bimetallic (CoFe-N-MPC) catalyst material performs slightly better (in terms of E_{onset} and $E_{1/2}$) than single metal counterparts, however, it still produces more peroxide than just iron-based material;
- introduction of manganese did not have an expected positive impact on cobalt-based material (CoMn-N-MPC vs. Co-N-MPC), at least in such low amounts of metals used in this work (ca. 1 wt%);
- introduction of manganese to iron-based material did not change the ORR activity, but slightly improved the stability of the material.

When looking at disc electrode data (Fig. 5a), then the CoFe-N-MPC material is the best performing, although both Fe-N-MPC and FeMn-N-MPC are rather close. The good electrocatalytic performance of these three materials is due to the coexistence of several ORR-active N moieties and M-N_x centres as well as suitable porous structure with defect-rich nature.

The role of M-N_x active centres in ORR electrocatalysis is well studied. For example, since Fe-N₄ moieties are covalently bonded to the carbon structure, the electron-donating or -withdrawing nature of the carbon support coming from delocalized π -electron system facilitates the chemisorption of O_2 and reaction intermediates with the metal centre [87]. Similar effect applies to the bimetallic catalysts as well and according to the DFT calculations, the respective centres possess

synergistic effects, which further improve the performance. For instance, Gong et al. found that the rate-determining step of the ORR on FeMn catalyst (protonation of O^*) has lower energy barrier than on monometallic catalyst according to the computed free energy diagrams [88]. Chen et al. showed from DFT calculations that FeCo has higher ORR activity than Fe and Co in Fe-N₄ and Co-N₄, respectively. Additionally, the Bader charge diagram showed significant change of the charge when both Fe and Co are introduced to the carbon framework [64].

Another aspect is the formation of HO_2^- during the ORR, since it can poison the metal-containing active sites as well as lowers the fuel cell's efficiency and power [62]. The results obtained herein indeed proved that cobalt-based catalyst materials facilitate peroxide production, whilst iron-based ones show significantly lower HO_2^- yields (also in combination with manganese) [59]. Additionally, as cobalt is considered a critical raw material by the European Commission [89], then it should be applied with caution, thus meaning cobalt-based materials have no advantages over iron-based counterparts.

3.3. Anion-exchange membrane fuel cell tests

Although the catalyst materials showed excellent electrocatalytic activity towards the ORR in alkaline media during the half-cell testing, it is important to evaluate whether this good ORR performance also carries on in anion-exchange membrane fuel cell application. Fe-N-MPC and FeMn-N-MPC catalysts were applied on the cathode side as these two showed the best performance, the lowest HO_2^- yield, and are free of critical raw materials. For MEA preparation non-PGM cathode materials were combined with Pt-Ru/C anode catalyst and HMT-PMBI based anion-exchange membrane. The AEMFC testing results are shown in Fig. 8. For comparison, commercial Pt/C (46 wt%) catalyst was also used on the cathode side. Similarly to the RRDE results, both Fe-N-MPC and FeMn-N-MPC showed almost identical behaviour and impressive fuel cell performance as the obtained peak power densities (P_{max}) were 473 and 474 mW cm^{-2} , and current densities at 0.75 V were 391 and 372 mA cm^{-2} , respectively. Both of these performances were superior to the MEA applying Pt/C cathode catalyst ($P_{\text{max}} = 328 \text{ mW cm}^{-2}$, $j_{0.75 \text{ V}} = 315 \text{ mA cm}^{-2}$).

With different operating conditions and materials (e.g. AEM, cell temperature, gas flow rate, etc.) being applied, the comparison with literature is quite difficult [90]. However, still it can be said that the Fe-N-MPC and FeMn-N-MPC catalyst materials are performing rather well when comparing with other iron-based materials reported in the literature (Table 5). Although there are also catalyst materials which have shown better performance [62,83,91,92], it should be noted that the AEM used is different. Whilst looking at the AEMFC performances, where the HMT-PMBI membrane was applied, then the results obtained in this study are superior.

Excellent AEMFC performance with Fe-N-MPC and FeMn-N-MPC cathode catalysts could be due to the combination of mesoporous

Table 5
Comparison of H_2/O_2 AEMFCs (operated at 60°C) using iron-based cathode catalysts.

Cathode catalyst	Cathode loading (mg cm^{-2})	Anode loading (mg cm^{-2})	Membrane	P_{max} (mW cm^{-2})	$j_{0.75 \text{ V}^*}$ (mA cm^{-2})	Ref.
Fe-N-MPC	2	0.8 Pt-Ru	HMT-PMBI	473	391	This work
FeMn-N-MPC				474	372	
Fe/IL-PAN-A1000	2	0.6 Pt-Ru	HMT-PMBI	289	150	[57]
Fe-N-Gra	2	0.6 Pt-Ru	HMT-PMBI	243	200	[54]
Fe-N-C	2	0.6 Pt-Ru	HMT-PMBI	220	260	[60]
FeN-SiCDC-0.5-400-wet-PVP	2	0.8 Pt-Ru	HMT-PMBI	356	390	[39]
FeCoNC	2	0.6 Pt-Ru	HMT-PMBI	415	300	[40]
Fe/N/CNT	2	0.4 Pt-Ru	<i>a</i> QAPS-S ₈	490	150	[96]
CoFe/VC	2.4	0.7 Pt-Ru	ETFE	1350	260	[91]
Fe _{0.5} -NH ₃	1.5	0.9 Pt-Ru	ETFE	1100	500	[62]
α -Mn ₂ O ₃ /Fe _{0.5} -NH ₃	1.2 (FeNC)	0.9 Pt-Ru	ETFE	1000	600	[62]
Fe-Co-N-C	1	1 Pt-Ru/C	LDPE	420	80	[97]

*Estimated from the Figures if value was not given at that potential

structure and presence of ORR-active sites, including the Fe-N₄ moieties. The mesoporous nature (pore diameters of 7–8 nm and 25–35 nm) of these catalysts is beneficial for the transport of reactants, making the embedded active sites accessible during the AEMFC operation. Such larger pores, especially those in the range of 25–35 nm, are less likely to be blocked by ionomer or liquid water, thus mesopores are responsible for the mass-transport of reactants and products through the catalyst layer [71,83,93]. As active sites, the Fe-N-MPC and FeMn-N-MPC materials both contain a mixture of different nitrogen moieties according to XPS, whose coexistence seems to be useful indeed. These iron-containing materials also have Fe-N_x active sites as XPS showed the presence of M-N_x moieties in both materials and no large metal agglomerates being visible from STEM studies, thus meaning iron might be atomically dispersed. While the role of other nitrogen moieties is arguable in the literature, the Fe-N₄ sites are rather agreed on to be ORR-active, promoting the 4e[−] pathway [59,93,94]. During the ORR on Fe-N₄, iron atom shifts slightly out of graphitic plane when O₂ molecule approaches, following chemisorption of O₂ on the Fe centre via an inner-sphere mechanism [87,94]. The presence of Fe-N_x sites might be the reason for low (<5%) yields of HO₂[−] on Fe-N-MPC and FeMn-N-MPC at practical potentials (>0.65 V) [95]. All in all, the results obtained suggest that Fe-N-MPC and FeMn-N-MPC materials could serve as potential cathode catalysts in the AEMFC application.

4. Conclusions

A novel commercially available mesoporous carbon-based engineered catalyst support was employed to prepare M-N-C type catalyst materials. High-temperature pyrolysis at 800 °C in the presence of 1,10-phenanthroline and transition metal (Fe, Co, Mn) acetates yielded five catalyst materials: Fe-N-MPC, Co-N-MPC, CoFe-N-MPC, FeMn-N-MPC and CoMn-N-MPC. All the prepared materials have rather homogeneous and highly porous structure according to SEM, the specific surface areas in the range of 550 m² g^{−1} and predominantly smaller (7–8 nm) and larger (25–35 nm) mesopores as determined by the N₂ physisorption analysis. The transition metal content in all catalyst materials was around 1 wt% according to MP-AES and SEM-EDX analysis with no large metal-containing particles visible and metals being well distributed in the materials as shown by STEM results. The XPS analysis showed the nitrogen content of 2.2–2.4 at% and the presence of different nitrogen moieties, namely pyridinic-N, pyrrolic-N, graphitic-N and M-N_x, on the catalyst surface, whose coexistence is considered to be useful. The RRDE studies revealed that the prepared catalyst materials exhibit excellent ORR activity in alkaline media with half-wave potentials up to 0.90 V. Co-N-MPC and CoMn-N-MPC materials have the highest yield of HO₂[−], followed by CoFe-N-MPC, and Fe-N-MPC and FeMn-N-MPC both have the lowest yield. Three best-performing catalysts, Fe-N-MPC, CoFe-N-MPC, and FeMn-N-MPC showed excellent stability after 10,000 potential cycles with only slight changes of the peroxide yield. The Fe-N-MPC and FeMn-N-MPC materials, which possessed the best electrocatalytic activity towards the ORR and the lowest HO₂[−] yield, were applied as cathode catalysts in an AEMFC. Both of them exhibited excellent and virtually the same fuel cell performance by reaching peak power densities of 473 and 474 mW cm^{−2}, respectively. However, after the short-term stability testing, the peroxide production slightly increased in case of Fe-N-MPC whereas no significant change was observed for FeMn-N-MPC, thereby suggesting better suitability of FeMn-N-MPC for practical application in AEMFC configuration.

CRediT authorship contribution statement

Jaana Lilloja: Investigation, Methodology, Writing – original draft, Writing – review & editing. **Elo Kibena-Pöldsepp:** Investigation, Supervision, Methodology, Writing – review & editing. **Ave Sarapuu:** Investigation, Supervision, Methodology, Writing – review & editing. **Maike Käärik:** Investigation, Methodology, Formal analysis.

Jekaterina Kozlova: Investigation, Methodology, Formal analysis, Writing – review & editing. **Päärn Paiste:** Investigation, Methodology, Formal analysis. **Arvo Kikas:** Investigation, Methodology, Formal analysis. **Alexey Treshchalov:** Investigation, Methodology, Formal analysis. **Jaan Leis:** Supervision, Methodology. **Aile Tamm:** Resources, Supervision, Methodology. **Vambola Kisand:** Supervision, Methodology. **Steven Holdcroft:** Methodology, Resources. **Kaido Tammeveski:** Conceptualization, Resources, Supervision, Writing – review & editing.

Declaration of Competing Interest

The authors declare that they have no known competing financial interests or personal relationships that could have appeared to influence the work reported in this paper.

Acknowledgements

The present work was financially supported by the Estonian Research Council (grants PRG723, PRG4). This research was also supported by the EU through the European Regional Development Fund (TK141, “Advanced materials and high-technology devices for energy recuperation systems”; TK134, “Emerging orders in quantum and nanomaterials” and TK143, “Molecular Cell Engineering”).

Appendix A. Supporting information

Supplementary data associated with this article can be found in the online version at doi:10.1016/j.apcatb.2022.121113.

References

- [1] H. Nazir, C. Louis, S. Jose, J. Prakash, N. Muthuswamy, M.E.M. Buan, C. Flox, S. Chavan, X. Shi, P. Kauranen, T. Kallio, G. Maia, K. Tammeveski, N. Lymeropoulos, E. Carcadea, E. Veziroglu, A. Iranzo, A.M. Kannan, Is the H₂ economy realizable in the foreseeable future? Part I: H₂ production methods, *Int. J. Hydrol. Energy* 45 (2020) 13777–13788.
- [2] H. Nazir, N. Muthuswamy, C. Louis, S. Jose, J. Prakash, M.E. Buan, C. Flox, S. Chavan, X. Shi, P. Kauranen, T. Kallio, G. Maia, K. Tammeveski, N. Lymeropoulos, E. Carcadea, E. Veziroglu, A. Iranzo, A.M. Kannan, Is the H₂ economy realizable in the foreseeable future? Part II: H₂ storage, transportation, and distribution, *Int. J. Hydrol. Energy* 45 (2020) 20693–20708.
- [3] H. Nazir, N. Muthuswamy, C. Louis, S. Jose, J. Prakash, M.E.M. Buan, C. Flox, S. Chavan, X. Shi, P. Kauranen, T. Kallio, G. Maia, K. Tammeveski, N. Lymeropoulos, E. Carcadea, E. Veziroglu, A. Iranzo, A.M. Kannan, Is the H₂ economy realizable in the foreseeable future? Part III: H₂ usage technologies, applications, and challenges and opportunities, *Int. J. Hydrol. Energy* 45 (2020) 28217–28239.
- [4] J.O. Abe, A.P.I. Popoola, E. Ajenifaju, O.M. Popoola, Hydrogen energy, economy and storage: review and recommendation, *Int. J. Hydrol. Energy* 44 (2019) 15072–15086.
- [5] M.K. Debe, Electrocatalyst approaches and challenges for automotive fuel cells, *Nature* 486 (2012) 43–51.
- [6] B.G. Pollet, S.S. Kocha, I. Staffell, Current status of automotive fuel cells for sustainable transport, *Curr. Opin. Electrochem.* 16 (2019) 90–95.
- [7] B. Tanc, H.T. Arat, E. Baltacioglu, K. Aydin, Overview of the next quarter century vision of hydrogen fuel cell electric vehicles, *Int. J. Hydrol. Energy* 44 (20) (2019) 10120–10128.
- [8] I. Staffell, D. Scaman, A.V. Abad, P. Balcombe, P.E. Dodds, P. Ekins, N. Shah, K. R. Ward, The role of hydrogen and fuel cells in the global energy system, *Energy Environ. Sci.* 12 (2019) 463–491.
- [9] S. Hussain, H. Erikson, N. Kongi, A. Sarapuu, J. Solla-Gullón, G. Maia, A. M. Kannan, N. Alonso-Vante, K. Tammeveski, Oxygen reduction reaction on nanostructured Pt-based electrocatalysts: a review, *Int. J. Hydrol. Energy* 45 (2020) 31775–31797.
- [10] L. Wang, X. Wan, S.Y. Liu, L. Xu, J.L. Shui, Fe-N-C catalysts for PEMFC: progress towards the commercial application under DOE reference, *J. Energy Chem.* 39 (2019) 77–87.
- [11] S. Akula, M. Mooste, B. Zulevi, S. McKinney, A. Kikas, H.-M. Piirsoo, M. Rähn, A. Tamm, V. Kisand, A. Serov, E.B. Creel, D.A. Cullen, K.C. Neyerlin, H. Wang, M. Odgaard, T. Reshetenko, K. Tammeveski, Mesoporous textured Fe-N-C electrocatalysts as highly efficient cathodes for proton exchange membrane fuel cells, *J. Power Sources* 520 (2022), 230819.
- [12] T. Asset, P. Atanassov, Iron-nitrogen-carbon catalysts for proton exchange membrane fuel cells, *Joule* 4 (2020) 33–44.
- [13] S. Gottesfeld, D.R. Dekel, M. Page, C. Bae, Y.S. Yan, P. Zelenay, Y.S. Kim, Anion exchange membrane fuel cells: current status and remaining challenges, *J. Power Sources* 375 (2018) 170–184.

[14] D.R. Dekel, Review of cell performance in anion exchange membrane fuel cells, *J. Power Sources* 375 (2018) 158–169.

[15] W.E. Mustain, Understanding how high-performance anion exchange membrane fuel cells were achieved: component, interfacial, and cell-level factors, *Curr. Opin. Electrochem.* 12 (2018) 233–239.

[16] X.Y. Luo, A. Wright, T. Weissbach, S. Holdcroft, Water permeation through anion exchange membranes, *J. Power Sources* 375 (2018) 442–451.

[17] E.S. Davydova, S. Mukerjee, F. Jaouen, D.R. Dekel, Electrocatalysts for hydrogen oxidation reaction in alkaline electrolytes, *ACS Catal.* 8 (2018) 6665–6690.

[18] D.R. Dekel, Unraveling mysteries of hydrogen electroxidation in anion exchange membrane fuel cells, *Curr. Opin. Electrochem.* 12 (2018) 182–188.

[19] A. Roy, M.R. Talarposhti, S.J. Normile, I.V. Zenyuk, V. De Andrade, K. Artyushkova, A. Serov, P. Atanassov, Nickel-copper supported on a carbon black hydrogen oxidation catalyst integrated into an anion-exchange membrane fuel cell, *Sustain. Energy Fuels* 2 (2018) 2268–2275.

[20] A. Sarapuu, E. Kibena-Pöldsepp, M. Borgheli, K. Tammeveski, Electrocatalysis of oxygen reduction on heteroatom-doped nanocarbons and transition metal–nitrogen–carbon catalysts for alkaline membrane fuel cells, *J. Mater. Chem. A* 6 (2018) 776–804.

[21] J. Lilloja, E. Kibena-Pöldsepp, M. Merisalu, P. Rauwel, L. Matisen, A. Niilisk, E.S. F. Cardoso, G. Maia, V. Sammelselg, K. Tammeveski, An oxygen reduction study of graphene-based nanomaterials of different origin, *Catalysts* 6 (2016) 108.

[22] I. Kruusenberg, J. Leis, M. Arulepp, K. Tammeveski, Oxygen reduction on carbon nanomaterial-modified glassy carbon electrodes in alkaline solution, *J. Solid State Electrochem.* 14 (2010) 1269–1277.

[23] I. Palm, E. Kibena-Pöldsepp, J. Lilloja, M. Käärik, A. Kikas, V. Kisand, M. Merisalu, A. Treshchalov, P. Paiste, J. Leis, A. Tamm, V. Sammelselg, K. Tammeveski, Impact of ball-milling of carbide-derived carbons on the generation of hydrogen peroxide via electroreduction of oxygen in alkaline media, *J. Electroanal. Chem.* 878 (2020), 114690.

[24] Z.X. Wu, M. Song, J. Wang, X. Liu, Recent progress in nitrogen-doped metal-free electrocatalysts for oxygen reduction reaction, *Catalysts* 8 (2018) 196.

[25] P. Zhang, F. Sun, Z.H. Xiang, Z.G. Shen, J. Yun, D.P. Cao, ZIF-derived in situ nitrogen-doped porous carbons as efficient metal-free electrocatalysts for oxygen reduction reaction, *Energy Environ. Sci.* 7 (2014) 442–450.

[26] J. Lilloja, E. Kibena-Pöldsepp, A. Sarapuu, A. Kikas, V. Kisand, M. Käärik, M. Merisalu, A. Treshchalov, J. Leis, V. Sammelselg, Q.L. Wei, S. Holdcroft, K. Tammeveski, Nitrogen-doped carbide-derived carbon/carbon nanotube composites as cathode catalysts for anion exchange membrane fuel cell application, *Appl. Catal. B* 272 (2020), 119012.

[27] L. Chen, C.Y. Xu, R. Du, Y.Y. Mao, C. Xue, L.M. Chen, L.T. Qu, J. Zhang, T. Yi, Rational design of three-dimensional nitrogen-doped carbon nanoleaf networks for high-performance oxygen reduction, *J. Mater. Chem. A* 3 (2015) 5617–5627.

[28] Z. Yang, Z. Yao, G.F. Li, G.Y. Fang, H.G. Nie, Z. Liu, X.M. Zhou, X. Chen, S. M. Huang, Sulfur-doped graphene as an efficient metal-free cathode catalyst for oxygen reduction, *ACS Nano* 6 (2012) 205–211.

[29] W.Q. Li, D.G. Yang, H.B. Chen, Y. Gao, H.M. Li, Sulfur-doped carbon nanotubes as catalysts for the oxygen reduction reaction in alkaline medium, *Electrochim. Acta* 165 (2015) 191–197.

[30] R. Sibul, E. Kibena-Pöldsepp, U. Mäeorg, M. Merisalu, A. Kikas, V. Kisand, A. Treshchalov, V. Sammelselg, K. Tammeveski, Sulphur and nitrogen co-doped graphene-based electrocatalysts for oxygen reduction reaction in alkaline medium, *Electrochim. Commun.* 109 (2019), 106603.

[31] D.S. Yang, D. Bhattacharyya, S. Inamdar, J. Park, J.S. Yu, Phosphorus-doped ordered mesoporous carbons with different lengths as efficient metal-free electrocatalysts for oxygen reduction reaction in alkaline media, *J. Am. Chem. Soc.* 134 (2012) 16127–16130.

[32] R. Li, Z.D. Wei, X.L. Gou, W. Xu, Phosphorus-doped graphene nanosheets as efficient metal-free oxygen reduction electrocatalysts, *RSC Adv.* 3 (2013) 9978–9984.

[33] M. Borgheli, N. Laocharoen, E. Kibena-Pöldsepp, L.S. Johansson, J. Campbell, E. Kauppinen, K. Tammeveski, O.J. Rojas, Porous N,P-doped carbon from coconut shells with high electrocatalytic activity for oxygen reduction: alternative to Pt-C for alkaline fuel cells, *Appl. Catal. B* 204 (2017) 394–402.

[34] I. Palm, E. Kibena-Pöldsepp, U. Mäeorg, J. Kozlova, M. Käärik, A. Kikas, J. Leis, V. Kisand, A. Tamm, K. Tammeveski, Silicon carbide-derived carbon electrocatalysts dual doped with nitrogen and phosphorus for the oxygen reduction reaction in an alkaline medium, *Electrochim. Commun.* 125 (2021), 106976.

[35] H.M. Fruehwald, I.I. Ebralidze, O.V. Zenkina, E.B. Easton, Effect of transition metals on the oxygen reduction reaction activity at metal-N₃/C active sites, *ChemElectroChem* 8 (2021) 53–61.

[36] O.Y. Bisen, K.K. Nanda, Alkaline earth metal based single atom catalyst for the highly durable oxygen reduction reaction, *Appl. Mater. Today* 21 (2020), 100846.

[37] O.Y. Bisen, A.K. Yadav, K.K. Nanda, Self-organized single-atom tungsten supported on the n-doped carbon matrix for durable oxygen reduction, *ACS Appl. Mater. Interfaces* 12 (2020) 43586–43595.

[38] G. Wu, A. Santandreu, W. Kellogg, S. Gupta, O. Ogoke, H.G. Zhang, H.L. Wang, L. M. Dai, Carbon nanocomposite catalysts for oxygen reduction and evolution reactions: from nitrogen doping to transition-metal addition, *Nano Energy* 29 (2016) 83–110.

[39] S. Rato, A. Zitolo, M. Käärik, M. Merisalu, A. Kikas, V. Kisand, M. Rähn, P. Paiste, J. Leis, V. Sammelselg, S. Holdcroft, F. Jaouen, K. Tammeveski, Non-precious metal cathodes for anion exchange membrane fuel cells from ball-milled iron and nitrogen doped carbide-derived carbons, *Renew. Energy* 167 (2021) 800–810.

[40] K. Kisand, A. Sarapuu, D. Danilian, A. Kikas, V. Kisand, M. Rähn, A. Treshchalov, M. Käärik, M. Merisalu, P. Paiste, J. Aruväli, J. Leis, V. Sammelselg, S. Holdcroft, K. Tammeveski, Transition metal-containing nitrogen-doped nanocarbon catalysts derived from 5-methylresorcinol for anion exchange membrane fuel cell application, *J. Colloid Interface Sci.* 584 (2021) 263–274.

[41] J. Lilloja, E. Kibena-Pöldsepp, A. Sarapuu, M. Kodali, Y. Chen, T. Asset, M. Käärik, M. Merisalu, P. Paiste, J. Aruväli, A. Treshchalov, M. Rähn, J. Leis, V. Sammelselg, S. Holdcroft, P. Atanassov, K. Tammeveski, Cathode catalysts based on cobalt and nitrogen-doped nanocarbon composites for anion exchange membrane fuel cells, *ACS Appl. Energy Mater.* 3 (2020) 5375–5384.

[42] O.Y. Bisen, R. Nandan, A.K. Yadav, B. Pavithra, K.K. Nanda, In situ self-organization of uniformly dispersed Co-N-C centers at moderate temperature without a sacrificial subsidiary metal, *Green Chem.* 23 (2021) 3115–3126.

[43] S. Kattel, P. Atanassov, B. Kiefer, Catalytic activity of Co-N_x/C electrocatalysts for oxygen reduction reaction: a density functional theory study, *Phys. Chem. Chem. Phys.* 15 (2013) 148–153.

[44] K. Artyushkova, A. Serov, S. Rojas-Carbonell, P. Atanassov, Chemistry of multitudinous active sites for oxygen reduction reaction in transition metal–nitrogen–carbon electrocatalysts, *J. Phys. Chem. C* 119 (2015) 25917–25928.

[45] J.H. Zagal, S. Specchia, P. Atanassov, Mapping transition metal-MN4 macrocyclic complex catalysts performance for the critical reactivity descriptors, *Curr. Opin. Electrochem.* 27 (2021), 100683.

[46] K. Tammeveski, J.H. Zagal, Electrocatalytic oxygen reduction on transition metal macrocyclic complexes for anion exchange membrane fuel cell application, *Curr. Opin. Electrochem.* 9 (2018) 207–213.

[47] J. Govan, W. Orellana, J.H. Zagal, F. Tasca, Penta-coordinated transition metal macrocycles as electrocatalysts for the oxygen reduction reaction, *J. Solid State Electrochem.* 25 (2021) 15–31.

[48] C.Z. Loyola, G. Abarca, S. Ureta-Zanartu, C. Aliaga, J.H. Zagal, M.T. Sougrati, F. Jaouen, W. Orellana, F. Tasca, Insights into the electronic structure of Fe penta-coordinated complexes. Spectroscopic examination and electrochemical analysis for the oxygen reduction and oxygen evolution reactions, *J. Mater. Chem. A* 9 (2021) 23802–23816.

[49] M.P. Oyarzun, N. Silva, D. Cortes-Arriagada, J.F. Silva, I.O. Ponce, M. Flores, K. Tammeveski, D. Belanger, A. Zitolo, F. Jaouen, J.H. Zagal, Enhancing the electrocatalytic activity of Fe phthalocyanines for the oxygen reduction reaction by the presence of axial ligands: Pyridine-functionalized single-walled carbon nanotubes, *Electrochim. Acta* 398 (2021), 139263.

[50] J.H. Zagal, M.T.M. Koper, Reactivity descriptors for the activity of molecular MN4 catalysts for the oxygen reduction reaction, *Angew. Chem. Int. Ed.* 55 (2016) 14510–14521.

[51] R. Praats, M. Käärik, A. Kikas, V. Kisand, J. Aruväli, P. Paiste, M. Merisalu, A. Sarapuu, J. Leis, V. Sammelselg, J.C. Douglan, D.R. Dekel, K. Tammeveski, Electrocatalysis of oxygen on cobalt phthalocyanine-modified carbide-derived carbon/carbon nanotube composite catalysts, *J. Solid State Electrochem.* 25 (2021) 57–71.

[52] M. Mamlouk, S.M.S. Kumar, P. Gouerec, K. Scott, Electrochemical and fuel cell evaluation of Co based catalyst for oxygen reduction in anion exchange polymer membrane fuel cells, *J. Power Sources* 196 (2011) 7594–7600.

[53] K. Li, Y. Li, W.C. Peng, G.L. Zhang, F.B. Zhang, X.B. Fan, Bimetallic iron-cobalt catalysts and their applications in energy-related electrochemical reactions, *Catalysts* 9 (2019) 762.

[54] R. Sibul, E. Kibena-Pöldsepp, S. Rato, M. Kook, M.T. Sougrati, M. Käärik, M. Merisalu, J. Aruväli, P. Paiste, A. Treshchalov, J. Leis, V. Kisand, V. Sammelselg, S. Holdcroft, F. Jaouen, K. Tammeveski, Iron and nitrogen-doped graphene-based catalysts for fuel cell applications, *ChemElectroChem* 7 (2020) 1739–1747.

[55] H. Lee, M.J. Kim, T. Lim, Y.E. Sung, H.J. Kim, H.N. Lee, O.J. Kwon, Y.H. Cho, A facile synthetic strategy for iron, aniline-based non-precious metal catalysts for polymer electrolyte membrane fuel cells, *Sci. Rep.* 7 (2017) 8.

[56] X.G. Fu, Y.R. Liu, X.P. Cao, J.T. Jin, Q. Liu, J.Y. Zhang, FeCo-N_x embedded graphene as high performance catalysts for oxygen reduction reaction, *Appl. Catal. B* 130 (2013) 143–151.

[57] M. Mooste, E. Kibena-Pöldsepp, V. Vassiljeva, A. Kikas, M. Käärik, J. Kozlova, V. Kisand, M. Külaavir, S. Cavaliere, J. Leis, A. Krumme, V. Sammelselg, S. Holdcroft, K. Tammeveski, Electrospun polyacrylonitrile-derived Co or Fe containing nanofibre catalysts for oxygen reduction reaction at the alkaline membrane fuel cell cathode, *ChemCatChem* 12 (2020) 4568–4581.

[58] J. Lilloja, E. Kibena-Pöldsepp, A. Sarapuu, J.C. Douglan, M. Käärik, J. Kozlova, P. Paiste, A. Kikas, J. Aruväli, J. Leis, V. Sammelselg, D.R. Dekel, K. Tammeveski, Transition-metal-and nitrogen-doped carbide-derived carbon/carbon nanotube composites as cathode catalysts for anion-exchange membrane fuel cells, *ACS Catal.* 11 (2021) 1920–1931.

[59] Y.Y. Sun, L. Silvioli, N.R. Sahraie, W. Ju, J.K. Li, A. Zitolo, S. Li, A. Bagger, L. Arnarson, X.L. Wang, T. Moeller, D. Bernsmeier, J. Rossmeisl, F. Jaouen, P. Strasser, Activity-selectivity trends in the electrochemical production of hydrogen peroxide over single-site metal–nitrogen–carbon catalysts, *J. Am. Chem. Soc.* 141 (2019) 12372–12381.

[60] J. Lilloja, M. Mooste, E. Kibena-Pöldsepp, A. Sarapuu, B. Zulevi, A. Kikas, H. M. Piirsoo, A. Tamm, V. Kisand, S. Holdcroft, A. Serov, K. Tammeveski, Mesoporous iron–nitrogen co-doped carbon material as cathode catalyst for the anion exchange membrane fuel cell, *J. Power Sources* 208 (2021), 100052.

[61] K. Artyushkova, S. Rojas-Carbonell, C. Santoro, E. Weiler, A. Serov, R. Awais, R. R. Gokhale, P. Atanassov, Correlations between synthesis and performance of Fe-based PGM-free catalysts in acidic and alkaline media: evolution of surface chemistry and morphology, *ACS Appl. Energy Mater.* 2 (2019) 5406–5418.

[62] P.G. Santori, F.D. Speck, S. Cherevko, H.A. Firouzjaie, X. Peng, W.E. Mustain, F. Jaouen, High performance FeNC and Mn-oxide/FeNC layers for AEMFC cathodes, *J. Electrochem. Soc.* 167 (2020), 134505.

[63] F.Z. Li, P. Shi, J.T. Wu, X.M. Qi, Y. Liu, G.L. Li, Trace bimetallic iron/manganese Co-doped N-Ketjenblack carbon electrocatalyst for robust oxygen reduction reaction, *J. Electrochem. Soc.* 168 (2021), 060502.

[64] L.L. Chen, Y.L. Zhang, L.L. Dong, W.X. Yang, X.J. Liu, L. Long, C.Y. Liu, S.J. Dong, J.B. Jia, Synergistic effect between atomically dispersed Fe and Co metal sites for enhanced oxygen reduction reaction, *J. Mater. Chem. A* 8 (2020) 4369–4375.

[65] T.T. Gao, Z.Y. Jin, Y.J. Zhang, G.Q. Tan, H.Y. Yuan, D. Xiao, Coupling cobalt-iron bimetallic nitrides and N-doped multi-walled carbon nanotubes as high-performance bifunctional catalysts for oxygen evolution and reduction reaction, *Electrochim. Acta* 258 (2017) 51–60.

[66] M. Zhang, J.P. Gao, W. Hong, X.X. Wang, Q. Tian, Z.L. An, L.Y. Wang, H.D. Yao, Y. Liu, X.X. Zhao, H.X. Qiu, Bimetallic Mn and Co encased within bamboo-like N-doped carbon nanotubes as efficient oxygen reduction reaction electrocatalysts, *J. Colloid Interface Sci.* 537 (2019) 238–246.

[67] K.Q. Zhong, Y. Wang, Q.K. Wu, H.H. You, H.G. Zhang, M.H. Su, R.Y. Liang, J. L. Zuo, S.R. Yang, J.F. Tang, Highly conductive skeleton Graphitic-C₃N₄ assisted Fe-based metal-organic frameworks derived porous bimetallic carbon nanofiber for enhanced oxygen-reduction performance in microbial fuel cells, *J. Power Sources* 467 (2020), 228313.

[68] Z. Yan, H. Qi, X. Bai, K. Huang, Y.R. Chen, Q. Wang, Mn doping of cobalt oxynitride coupled with N-rGO nanosheets hybrid as a highly efficient electrocatalyst for oxygen reduction and oxygen evolution reaction, *Electrochim. Acta* 283 (2018) 548–559.

[69] P. Trogadas, T.F. Fuller, P. Strasser, Carbon as catalyst and support for electrochemical energy conversion, *Carbon* 75 (2014) 5–42.

[70] X. Liu, L.M. Dai, Carbon-based metal-free catalysts, *Nat. Rev. Mater.* 1 (2016) 16064.

[71] T. Soboleva, X.S. Zhao, K. Mallek, Z. Xie, T. Navessin, S. Holdcroft, On the micro-, meso- and macroporous structures of polymer electrolyte membrane fuel cell catalyst layers, *ACS Appl. Mater. Interfaces* 2 (2010) 375–384.

[72] F.A. Westerhaus, R.V. Jagadeesh, G. Wienhofer, M.M. Pohl, J. Radnik, A.E. Surkus, J. Rabeah, K. Junge, H. Junge, M. Nielsen, A. Bruckner, M. Beller, Heterogenized cobalt oxide catalysts for nitroarene reduction by pyrolysis of molecularly defined complexes, *Nat. Chem.* 5 (2013) 537–543.

[73] H.Z. Yang, L. Shang, Q.H. Zhang, R. Shi, G.I.N. Waterhouse, L. Gu, T.R. Zhang, A universal ligand mediated method for large scale synthesis of transition metal single atom catalysts, *Nat. Commun.* 10 (2019) 4585.

[74] A.G. Wright, J.T. Fan, B. Britton, T. Weissbach, H.F. Lee, E.A. Kitching, T. J. Peckham, S. Holdcroft, Hexamethyl-p-terphenyl poly(benzimidazolium): a universal hydroxide-conducting polymer for energy conversion devices, *Energy Environ. Sci.* 9 (2016) 2130–2142.

[75] M. Thommes, K. Kaneko, A.V. Neimark, J.P. Olivier, F. Rodriguez-Reinoso, J. Rouquerol, K.S.W. Sing, Physisorption of gases, with special reference to the evaluation of surface area and pore size distribution (IUPAC Technical Report), *Pure Appl. Chem.* 87 (2015) 1051–1069.

[76] B. Britton, S. Holdcroft, The control and effect of pore size distribution in AEMFC catalyst layers, *J. Electrochem. Soc.* 163 (2016) F353–F358.

[77] A.C. Ferrari, J. Robertson, Interpretation of Raman spectra of disordered and amorphous carbon, *Phys. Rev. B* 61 (2000) 14095–14107.

[78] A. Sadezky, H. Muckenhuber, H. Grothe, R. Niessner, U. Pöschl, Raman microspectroscopy of soot and related carbonaceous materials: spectral analysis and structural information, *Carbon* 43 (2005) 1731–1742.

[79] Y. Kouketu, T. Mizukami, H. Mori, S. Endo, M. Aoya, H. Hara, D. Nakamura, S. Wallis, A new approach to develop the Raman carbonaceous material geothermometer for low-grade metamorphism using peak width, *Isl. Arc* 23 (2014) 33–50.

[80] S. Kabir, K. Artyushkova, A. Serov, P. Atanassov, Role of nitrogen moieties in N-doped 3D-graphene nanosheets for oxygen electroreduction in acidic and alkaline media, *ACS Appl. Mater. Interfaces* 10 (2018) 11623–11632.

[81] L.F. Lai, J.R. Potts, D. Zhan, L. Wang, C.K. Poh, C.H. Tang, H. Gong, Z.X. Shen, L. Y. Jianyi, R.S. Ruoff, Exploration of the active center structure of nitrogen-doped graphene-based catalysts for oxygen reduction reaction, *Energy Environ. Sci.* 5 (2012) 7936–7942.

[82] I. Matanovic, K. Artyushkova, P. Atanassov, Understanding PGM-free catalysts by linking density functional theory calculations and structural analysis: perspectives and challenges, *Curr. Opin. Electrochem.* 9 (2018) 137–144.

[83] H. Adabi, A. Shakouri, N. Ul Hassan, J.R. Varcoe, B. Zulevi, A. Serov, J. R. Regalbuto, W.E. Mustain, High-performing commercial Fe-N-C cathode electrocatalyst for anion-exchange membrane fuel cells, *Nat. Energy* 6 (2021) 834–843.

[84] K. Kreek, A. Sarapuu, L. Samolberg, U. Joost, V. Mikli, M. Koel, K. Tammeveski, Cobalt-containing nitrogen-doped carbon aerogels as efficient electrocatalysts for the oxygen reduction reaction, *ChemElectroChem* 2 (2015) 2079–2088.

[85] U. Tylus, Q.Y. Jia, K. Strickland, N. Ramaswamy, A. Serov, P. Atanassov, S. Mukerjee, Elucidating oxygen reduction active sites in pyrolyzed metal-nitrogen coordinated non-precious-metal electrocatalyst systems, *J. Phys. Chem. C* 118 (2014) 8999–9008.

[86] M.S. Thorum, J.M. Hankett, A.A. Gewirth, Poisoning the oxygen reduction reaction on carbon-supported Fe and Cu electrocatalysts: evidence for metal-centered activity, *J. Phys. Chem. Lett.* 2 (2011) 295–298.

[87] N. Ramaswamy, U. Tylus, Q.Y. Jia, S. Mukerjee, Activity descriptor identification for oxygen reduction on nonprecious electrocatalysts: linking surface science to coordination chemistry, *J. Am. Chem. Soc.* 135 (2013) 15443–15449.

[88] S.P. Gong, C.L. Wang, P. Jiang, L. Hu, H. Lei, Q.W. Chen, Designing highly efficient dual-metal single-atom electrocatalysts for the oxygen reduction reaction inspired by biological enzyme systems, *J. Mater. Chem. A* 6 (2018) 13254–13262.

[89] S. Bobba, S. Carrara, J. Huisman, F. Mathieu, C. Pavel, Critical Raw Materials for Strategic Technologies and Sectors in the EU - A Foresight Study, 2020. <https://doi.org/10.2873/58081>.

[90] T.J. Omasta, L. Wang, X. Peng, C.A. Lewis, J.R. Varcoe, W.E. Mustain, Importance of balancing membrane and electrode water in anion exchange membrane fuel cells, *J. Power Sources* 375 (2018) 205–213.

[91] X. Peng, V. Kashyap, B. Ng, S. Kurungot, L.Q. Wang, J.R. Varcoe, W.E. Mustain, High-performing PGM-free AEMFC cathodes from carbon-supported cobalt ferrite nanoparticles, *Catalysts* 9 (2019) 264.

[92] H. Adabi, P.G. Santori, A. Shakouri, A. Peng, K. Yassin, I.G. Rasin, S. Brandon, D. R. Dekel, N.U. Hassan, M.-T. Sougrati, A. Zitolo, J.R. Varcoe, J.R. Regalbuto, F. Jaouen, W.E. Mustain, Understanding how single-atom site density drives the performance and durability of PGM-free Fe–N–C cathodes in anion exchange membrane fuel cells, *Mater. Today Adv.* 12 (2021), 100179.

[93] S. Specchia, P. Atanassov, J.H. Zagal, Mapping transition metal-nitrogen-carbon catalyst performance on the critical descriptor diagram, *Curr. Opin. Electrochem.* 27 (2021), 100687.

[94] H.A. Firouzjaie, W.E. Mustain, Catalytic advantages, challenges, and priorities in alkaline membrane fuel cells, *ACS Catal.* 10 (2019) 225–234.

[95] N. Ramaswamy, S. Mukerjee, Alkaline anion-exchange membrane fuel cells: challenges in electrocatalysis and interfacial charge transfer, *Chem. Rev.* 119 (2019) 11945–11979.

[96] H. Ren, Y. Wang, Y. Yang, X. Tang, Y.Q. Peng, H.Q. Peng, L. Xiao, J.T. Lu, H. D. Abruna, L. Zhuang, Fe/N/C nanotubes with atomic Fe sites: a highly active cathode catalyst for alkaline polymer electrolyte fuel cells, *ACS Catal.* 7 (2017) 6485–6492.

[97] L. Osmieri, C. Zafferoni, L.Q. Wang, A. Videla, A. Lavacchi, S. Specchia, Polypyrrole-derived Fe-Co-N-C catalyst for the oxygen reduction reaction: performance in alkaline hydrogen and ethanol fuel cells, *ChemElectroChem* 5 (2018) 1954–1965.